ADVANCED FUNCTIONAL MATERIALS

Supporting Information

for *Adv. Funct. Mater.*, DOI 10.1002/adfm.202308948

Chiral Recognition: A Spin-Driven Process in Chiral Oligothiophene. A Chiral-Induced Spin Selectivity (CISS) Effect Manifestation

*Andrea Stefani, Tommaso Salzillo, Patrizia Romana Mussini, Tiziana Benincori, Massimo Innocenti, Luca Pasquali, Andrew C. Jones, Suryakant Mishra and Claudio Fontanesi**

Supporting Information

Chiral recognition: a spin-driven process in chiral oligothiophene.

A chiral-induced spin selectivity (CISS) effect manifestation.

Andrea Stefani[1,2], Tommaso Salzillo[3], Patrizia Romana Mussini[4], Tiziana Benincori[5], Massimo Innocenti[6,7], Luca Pasquali[2,8,9], Andrew C. Jones[10], Suryakant Mishra[10,11], Claudio Fontanesi[2,7]*

[1]*Department of Physics, Informatics and Mathematics 'FIM', University of Modena and Reggio Emilia, Via Giuseppe Campi, 213, 41125 Modena, Italy*
[2]*Department of Engineering 'Enzo Ferrari', DIEF, University of Modena and Reggio Emilia, Via Vivarelli 10, 41125 Modena, Italy*
[3]*Department of Industrial Chemistry "Toso Montanari", University of Bologna, Viale del Risorgimento, 4, 40136 - Bologna, Italy.*
[4]*Department of Chemistry, University of Milano, Via Golgi 19, 20133 Milano, Italy*
[5] *Department of Science and Technology, DISAT, University of Insubria, Via Valleggio 11, 22100 Como, Italy*
[6] *Department of Chemistry, "Ugo Schiff", Univ. of Firenze, via della Lastruccia 3, 50019 Sesto Fiorentino, Italy.*
[7] *National Interuniversity Consortium of Materials Science and Technology (INSTM), Via G. Giusti 9, 50121 Firenze (FI), Italy.*
[8] *IOM-CNR, Strada Statale 14, Km. 163.5 in AREA Science Park, Basovizza, 34149 Trieste, Italy.*
[9] *Department of Physics, University of Johannesburg, P.O. Box 524, Auckland Park 2006, South Africa.*
[10]*Center for Integrated Nanotechnologies, Los Alamos National Laboratory, Los Alamos, NM 87545, USA*
[11]*Pritzker School of Molecular Engineering at University of Chicago, 5640 S Ellis Ave, Chicago, Illinois 60637, USA*

Index

1) Silver Nanoparticles (AgNPs): preparation and characterization.

In this section XPS and electrochemical results are reported concerning the characterization of BT_2T_4 capped AgNPs (BT_2T_4@AgNP).

1.1 Silver Nanoparticles: Synthesis and Characterization

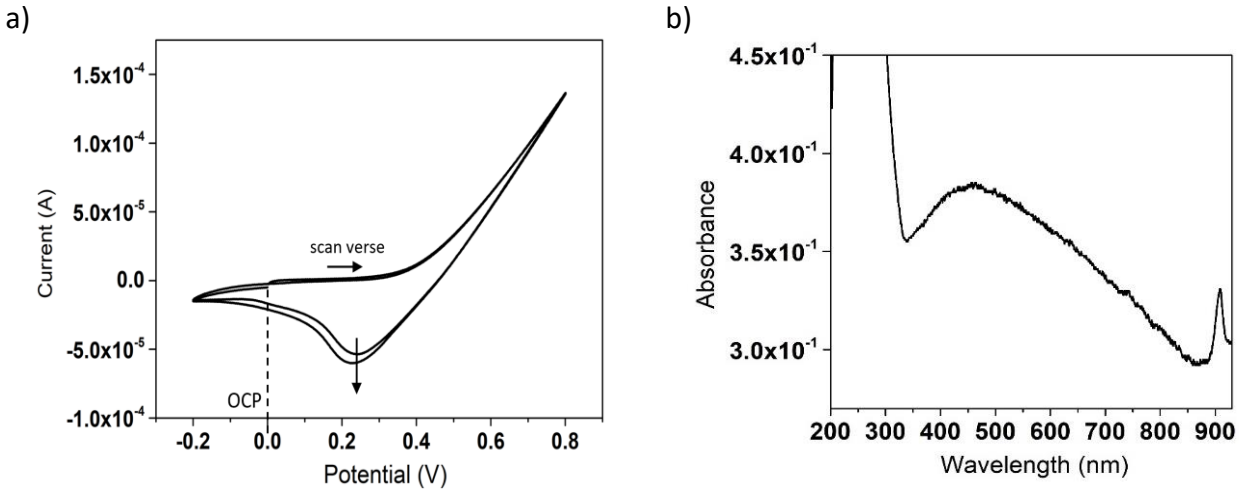

Figure S1. a) CV relevant to the AgNPs electrochemical synthesis. A silver wire serves as the WE in a 0.02 M $NaNO_3$ ethanol solution, 0.1 V s^{-1} is the potential scan rate. Pt and Ag/AgCl/KCl_{sat} served as the (CE) and (RE) electrodes respectively. b) UV-Vis absorption spectrum of the solution after electrochemical AgNPs production.[1]

Silver nanoparticles were electrochemically synthesized following the method of Starowicz *et al.* [2]. Fig. S1a shows the CVs relevat to the AgNPs preparation, in a $NaNO_3$ 0.02 M ethanol solution. Both the oxidation onset potential (0.35 V) and the reduction peak potential (0.22 V) are in tight agreement with the results reported in the literature.[2,3] The actual AgNPs synthesis was carried out under galvanostatic control: 30 minutes at a constant current of 0.14 mA (which corresponds to the current at 0.8 V potential, compare the CV in Fig. S1a). The freshly prepared AgNPs suspension was characterized via UV-Vis spectroscopy, the relevant spectra are reported in Figure S1b. The spectrum shows a broad and shallow peak centered at 420 nm, consistent with literature data, suggesting a AgNPs size distribution in the 20 to 50 nm range.[2,3] The presence of the nanoparticles in suspension was also cross-checked via a simple laser scattering experiment, Fig. S2, The cuvette closer to the laser contains the solution before the electrochemical production of AgNPs (blank solution), the cuvette closer to the white screen contains the solution after AgNPs electrochemical synthesis. The AgNPs presence is clearly seen in the AgNPs suspension due to scattering (allowing to "see" the green laser ray shone "through" the AgNPs suspension).

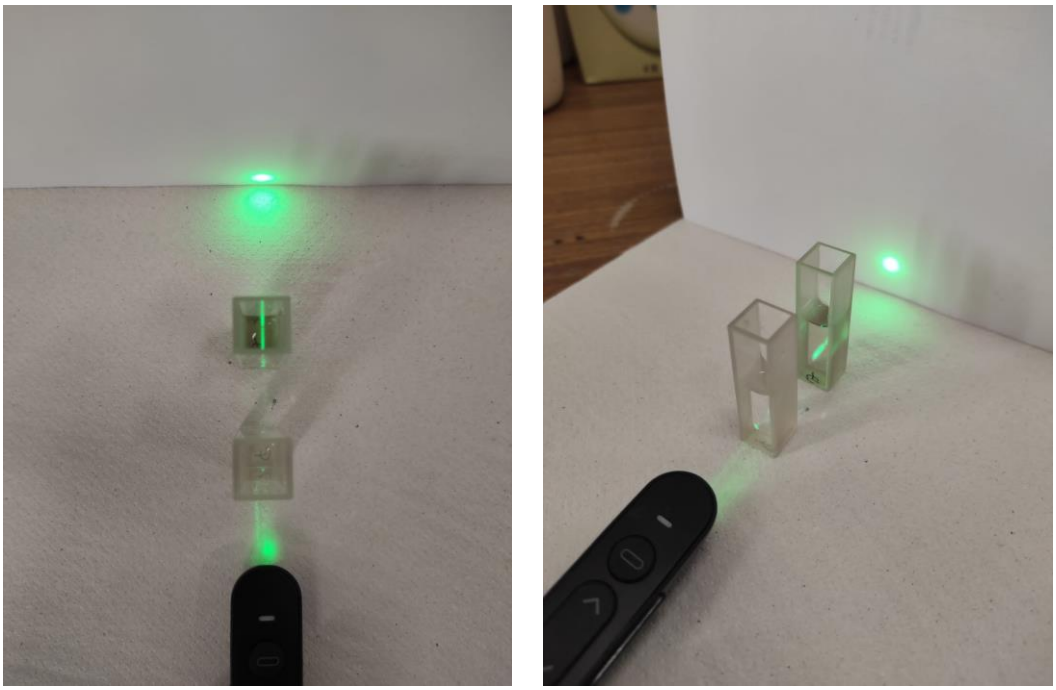

Figure S2. Laser scattering experiment, two cuvettes: the cuvette closer to the laser source contains the ethanolic solution prior AgNPs synthesis, while the cuvette closer to the screen is the AgNPs suspension after electrosynthesis.

1.2 BT_2T_4 capped AgNPs (BT_2T_4@AgNPs)

The electrochemically synthesized AgNPs are then chiralized by capping with enantiopure BT_2T_4 molecules (experimental section 4.5, main manuscript). XPS spectra have been recorded for BT_2T_4@AgNPs, to cross-check the effective functionalization. To this purpose, the most critical aspect of the XPS characterization is the investigation of the S 2p core level, which was included in the main manuscript (section 2.2.1). Figure S3 presents all the supplementary details concerning the XPS investigation of the BT_2T_4@AgNPs interface. Freshly synthesized BT_2T_4@AgNPs suspension was drop-casted on a glassy carbon substrate, and then dried under a nitrogen stream. The nanoparticles suspension was drop-casted on a glassy carbon surface in order to minimize any complication due to possible chemisorption on the substrate.

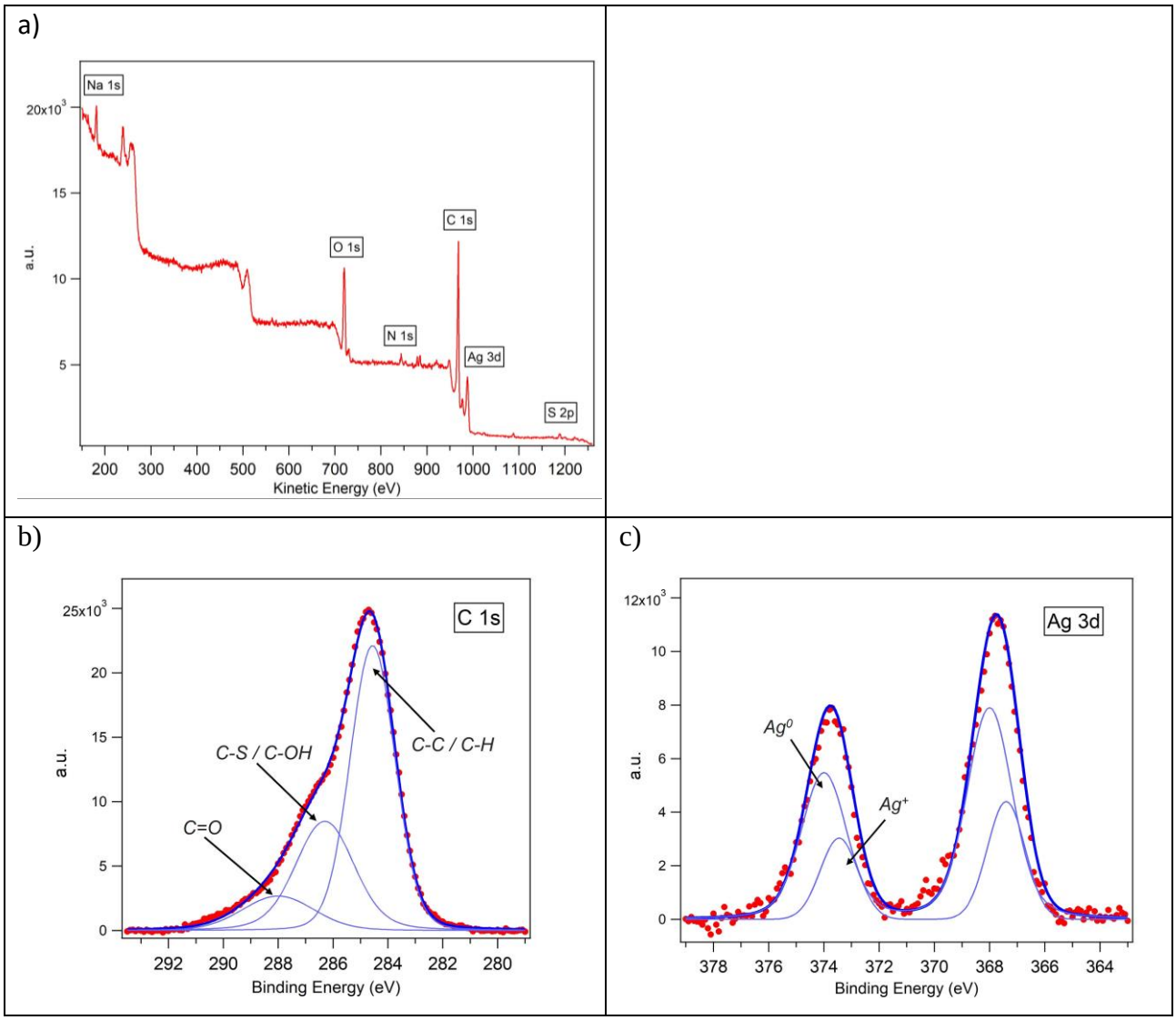

Figure S3. XPS spectra of a BT_2T_4@AgNPs suspension drop-casted on a glassy carbon surface, probed with Mg Kα X-ray source, 1.254 keV of photon energy. a) Survey spectrum. b) C 1s. c) Ag 3d. The dotted red curve represents the experimental spectra. The thick blue line curve are the overall fitted data (thin blue line curves are the individual components).

The survey spectrum (Fig. S3a) shows prominent peaks associated with silver and sulfur. The Ag 3d spectrum shown in Fig. S3c features two components with a very small energy splitting, of about 0.5 eV. The higher binding energy structure, 368.3 eV (Ag $3d_{5/2}$ peak), is assigned to metallic silver, while the lower energy structure, 367.7 eV, is due to silver cation, Ag^+. The presence of Ag^+ is possibly due to silver not reduced by ethanol, following the electrochemical oxidation.

1.3 Au|BT_2T_4|AgNPs

1.3.1 Au|BT_2T_4|AgNPs electrochemical measurements

AgNPs were exploited as a reversible redox couple to probe the charge transmission properties of the Au|BT_2T_4 interface. To this end, an Au|BT_2T_4|AgNPs multi-layered interface has been prepared via overnight incubation of Au|BT_2T_4 into the AgNPs suspension (details are reported in the experimental

section 4.4). It is expedient to assume that a strong chemical interaction occurs between Au|BT_2T_4 and AgNPs, via the dangling thiophene sulfur atoms oriented towards the solution. An assumption consistent with both XPS, Raman and theoretical results.

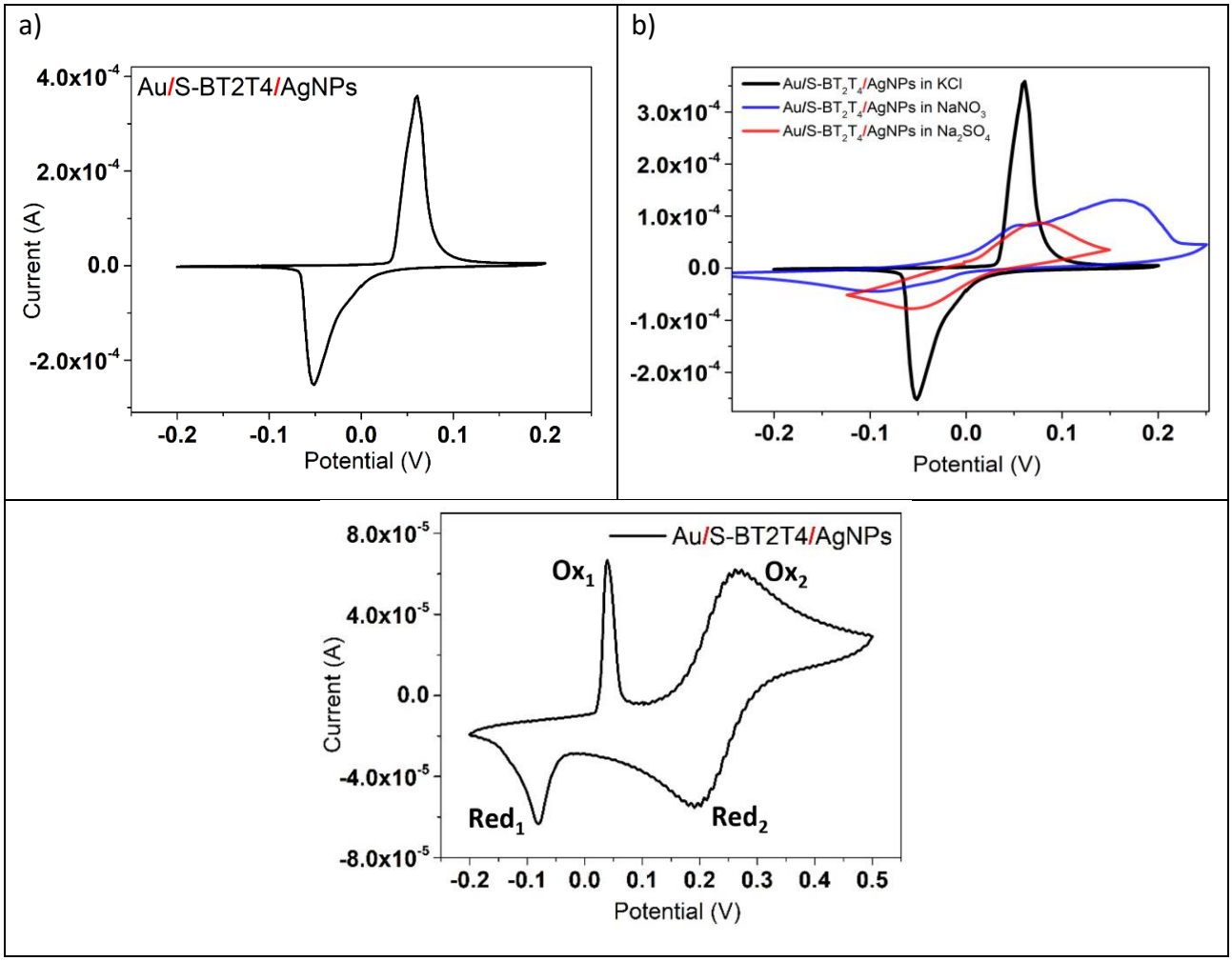

Figure S4. CV curves of the Au|BT_2T_4|AgNPs interface serving as the WE. a) 0.1 M KCl aqueous solution, 0.05 V s^{-1} potential scan rate. The potential is cycled in the -0.2 V to 0.2 V range, i.e. around the redox couple Ag/Ag^+ standard potential window. b) Comparison of the AgNPs redox signal using KCl as the supporting electrolyte (black line, same plot as panel a) and other electrolytes (blue line $NaNO_3$, red line Na_2SO_4) c) 5 mM Fe(III)|Fe(II) redox couple in 0.1 M KCl aqueous solution, 0.1 V s^{-1} potential scan rate.

Figure S4 shows cross-check CVs of the Au|S-BT_2T_4|AgNPs hybrid-interface, which serves as the WE. In particular, figure S4a is recorded in a 0.1 M KCl aqueous solution, at a 50 mV s^{-1} potential scan rate, two quasi-reversible current peaks are present in the CV, centered at about +0.075 V (oxidation regime, labelled as E_{ox} in Fig. S4a) and -0.075 V (reduction regime, labelled as E_{red} in Fig. S4a). The oxidation of silver with formation of silver chloride is the redox reaction underlying the oxidation peak, compare reaction (1). This result is confirmed by cross-check of CV measurements carried out in 0.3 M Na_2SO_4 and 0.1 M $NaNO_3$ water solution: the current peaks are

much more swallow and featuring an large peak to peak potential difference, in agreement with results in the literature.[4,5]

$$\mathrm{AgNPs_{adsorbed}} + \mathrm{Cl^-} \rightleftharpoons \mathrm{AgNPs_{adsorbed}} - \mathrm{Cl} + \mathrm{e^-} \qquad (1)$$

Please compare CVs in Figure S4b. Please take into account that reaction (1) is the reaction of the silver/silver chloride second species reference electrode (granting for a robust electrochemical stability). Figure S4c shows a CV curve where the Au|S-BT_2T_4|AgNPs interface serves as the WE, with the presence in solution of a 5 mM Fe(III)|Fe(II) redox couple, in a 0.1 M KCl aqueous solution, at 100 mV s^{-1} potential scan rate. In this case, both the Ag/Ag^+ (Ox_1 and Red_1 curret peaks) and the Fe^{3+}/Fe^{2+} (Ox_2 and Red_2 current peaks) one-electron reversible electrochemical processes are present, and they show clear-cut current peaks. The redox processes underlying the presence of the current peaks are shown below:

Ox₁: $Ag + Cl^- \rightarrow AgCl + e^-$ **Ox₂**: $Fe^{2+} \rightarrow Fe^{3+} + e^-$.

Red₁: $AgCl + e^- \rightarrow Ag + Cl^-$ **Red₂**: $Fe^{3+} + e^- \rightarrow Fe^{2+}$

1.3.2 Au|BT_2T_4@AgNPs XPS results

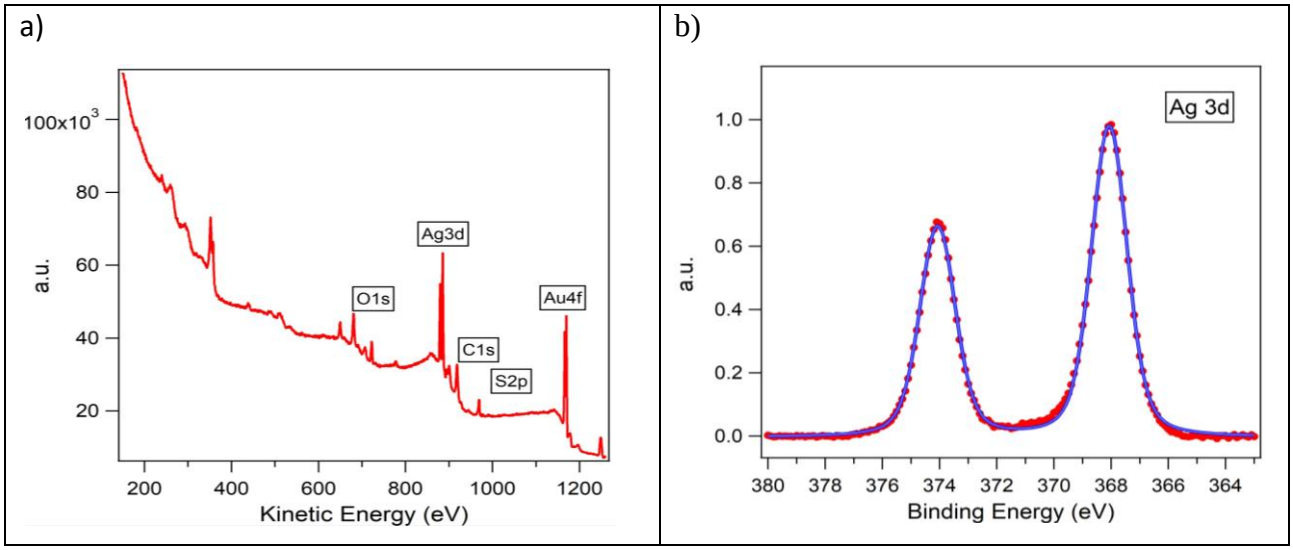

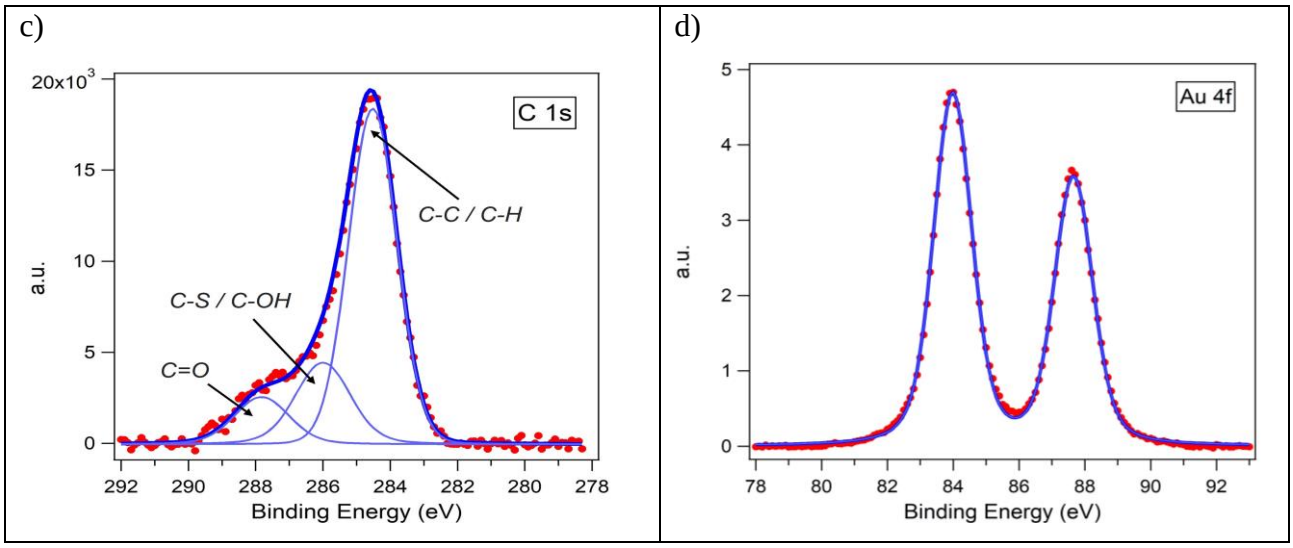

Figure S5. XPS spectra of the Au|BT_2T_4@AgNPs interface, Mg Kα photons, 1.254 keV photon energy. a) Survey spectrum b) Ag 3d c) C 1s d) Au 4f. The dotted red curve represents the experimental spectra. The thick blue line curve are the overall fitted data (thin blue line curves are the individual components).

Chemisorption of BT_2T_4 on AgNPs has been characterized recording XPS spectra of the Au|BT_2T_4@AgNPs interface. The survey scan and the relevant core levels are displayed in figure S5, except for the critical S 2p domain, main manuscript (section 2.2.1).

2) Gold surfaces: preparation and characterization.

Overnight incubation of gold surfaces in a freshly prepared enantiopure BT_2T_4 ethanolic solution allowed to obtain gold functionalized WE, details in the experimental section. A procedure also exploited to functionalize gold surfaces with thiol derivatives[6,7] Functionalized surfaces were characterized via XPS spectroscopy, electrodesorption experiments and Raman spectroscopy.

2.1 Au|BT_2T_4 XPS results

Fig. S6 shows XPS spectra of the Au|BT_2T_4 interface. Fig. S6 a, b, c show the survey scan, the C 1s and the Au 4f core levels, respectively. S 2p data are reported in the main manuscript (section 2.2.1).

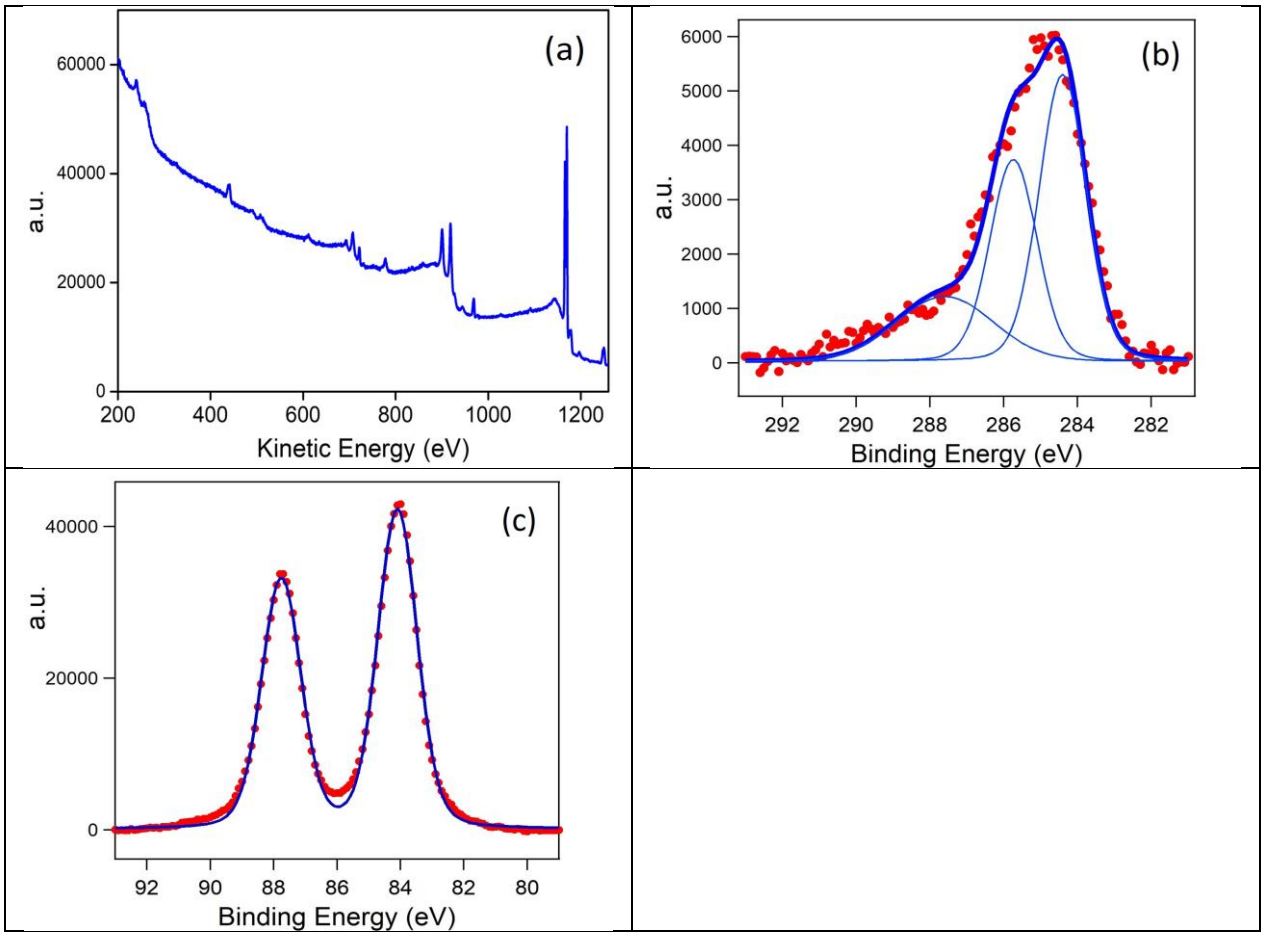

Fig. S6. XPS spectra of the Au|BT_2T_4interface, Mg Kα photons, 1.254 keV photon energy. a) Survey spectrum b) C 1s c) Au 4f. Dotted red curves are the experimental spectra. Thick blue line overall fit, thin blue line the fitted data individual components.

In the main manuscript, the S 2p domain is investigated with two different probing photons (Fig. 5b). The main spectrum is acquired with Mg Kα photons (1.254 keV); the inset spectrum is probed with 260 eV synchrotron light photons. Based on the Mg Kα XPS results, it is possible to estimate the effective film thickness from optical absorption of the BT_2T_4. Accounting also for the reflectivity of the gold surface, i.e. quantitative comparison, Au 4f spectra, of the bare and functionalized surface.[5,8] In fact, a 1.254 keV energy, of probing photons, corresponds to a high inelastic mean free path in the organic film: a value of Λ=30 Å ± 2 Å is expected for organic chemisorbed molecules.[9–11] Eq. (2) allows to determine the effective interface film thickness (d), for an estimated value of Λ ~ 30 Å:[4,12,13]

$$d \approx \Lambda \, ln\left(I_{Au_0}/I_{Au_d}\right) \quad (2)$$

where I_{Au_0} is the Au $4f_{7/2}$ bare gold surface intensity, I_{Au_d} is the intensity of the Au $4f_{7/2}$ photoelectrons attenuated by a homogeneous film of effective thickness d, and Λ is the inelastic mean free path of the photoelectrons within this layer. The estimated thickness of the BT_2T_4 SAM is 50 Å. This value is consistent with a surface coverage ranging between 1 and 1.5 monolayers.

2.2 Au|BT_2T_4|BT_2T_4@AgNPs enantio-recognition (Exp I reproducibility)

Figure S7 shows three physically different experiments which are the replica of Experiment I, this to assess the reproducibility of the whole synthesis and measurement procedure, from sample (interfaces) preparation to CV measurements concerning the electrochemical based chiral(enantio) recognition.

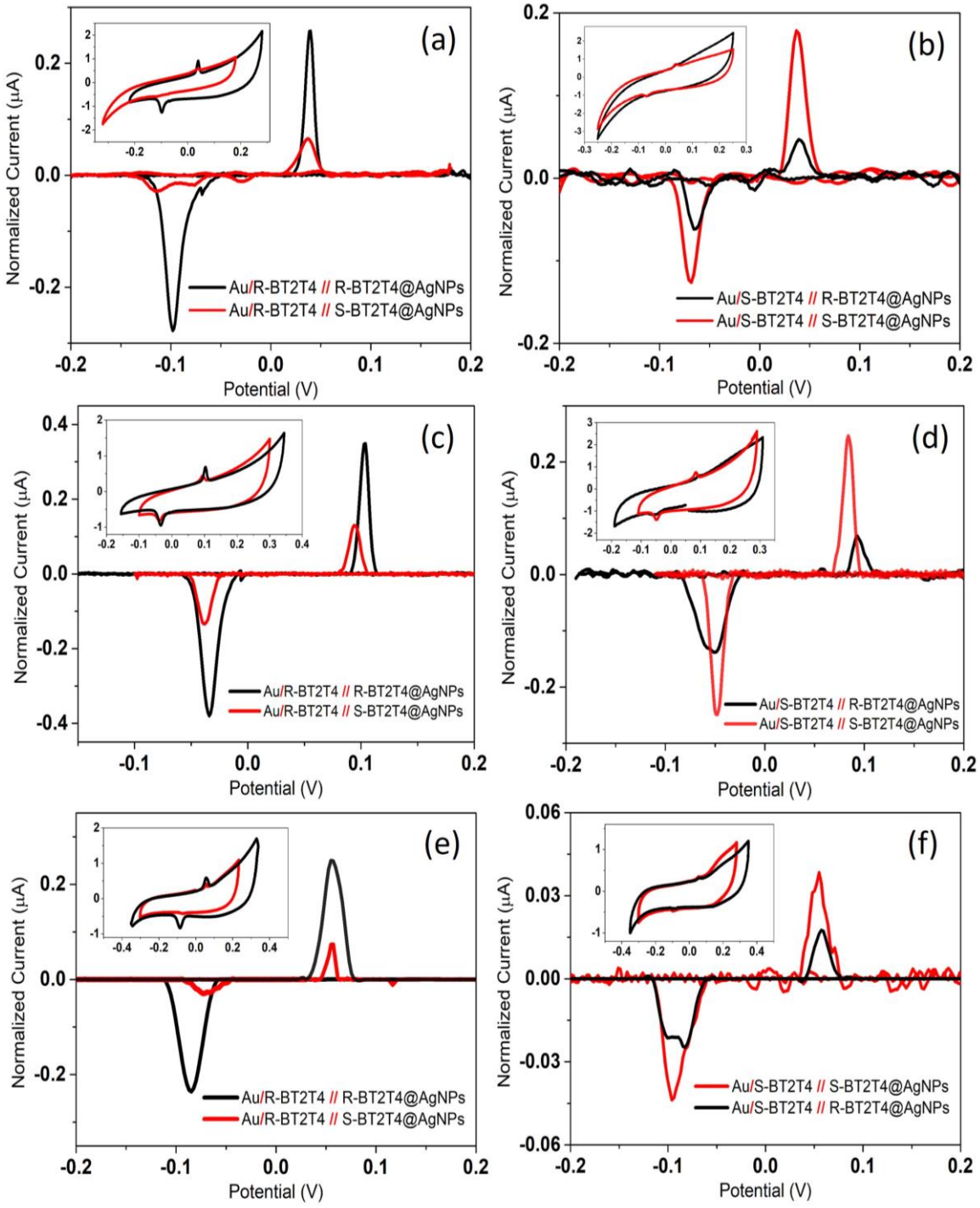

Figure S7. Physically different replica of the CVs of the main manuscript: Experiment I (chiral recognition electrochemistry). CVs are recorded for all the possible handedness combinations using different WEs (for the same preparation procedure). Main panels show the normalized current vs potential curves (baseline subtraction) while the insets display the raw data.

Based on the results shon in Figure 2 main manuscript and Figure S7 supporting information, we can conclude that CVs data relevant to Experiment I allow for a certain enantio recognition of the surface handedness exploiting the “chiralized AgNPs. From a quantitative point of view the deggre on uncertainty in both potential shift and peak current are around 5 %.

3) Raman spectroscopy: theoretical and experimental results

3.1 TD-DFT Raman spectra, single BT_2T_4 species

To account for Raman spectroscopy results collected by using two excitation laser energies: 514.5 nm and 785 nm excitation light sources, electronic spectra (TD-DFT) have been calculated. Fig. S8 shows BT_2T_4 TD-DFT spectra calculated at the B3LYP/cc-pVTZ level of the theory, for both the neutral (Fig. S8a) and cation (Fig. S8b) species. The lowest energy of absorption for the neutral form corresponds to 440 nm wavelength, whilst the cation has its maximum absorption in the 550 to 850 nm range. This is relevant to the results observed both for BT_2T_4 chemisorbed on Au and in “is-situ”/”in-operando” Raman spectra of BT_2T_4 chemisorbed on Ni (*vide infra*, sections 3.2 and 3.3).

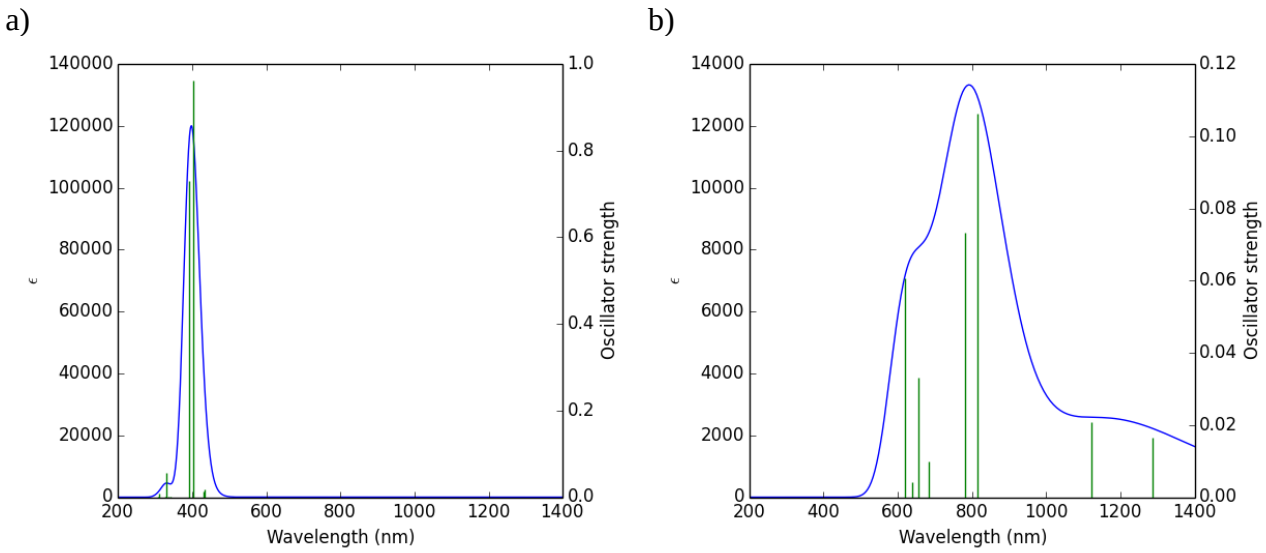

Fig S8. DFT UV-Vis spectra calculated at the BT_2T_4, B3LYP/cc-pVTZ level of the theory. a) neutral singlet. b) cation doublet.

Fig. S9 shows Raman spectra calculated at the B3LYP/cc-pVTZ level of the theory. Theoretical Raman spectra feature a significative large intensity peaks centered at around 1500 cm^{-1} and the two largest intensity peaks in the 1300 to 1400 and cm^{-1} range.

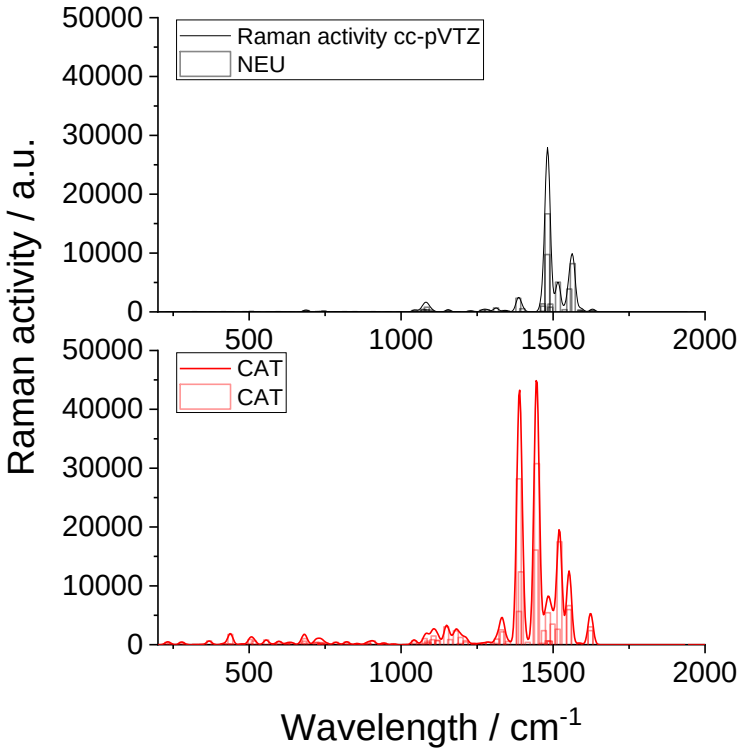

Fig S9. DFT Raman intensity calculated at the BT_2T_4, B3LYP/cc-pVTZ level of the theory. Black bars and curve neutral (NEU) species. Red bars and curves refer to the cation (CAT) species.

3.2 PM6 Au|BT_2T_4 Raman spectrum

Fig. S10 shows the Raman spectrum calculated for the BT_2T_4/Au57 cluster, three Au atoms in direct contact with the BT_2T_4 molecule are allowed to relax. Both satellite peaks at around 750 cm^{-1} and the prominent peaks at 1250 cm^{-1} are also found in the experimental spectrum of the Au|BT_2T_4 interface (vide infra, section 3.2), they are not evident in the neutral molecule (Fig S9). The calculated Mulliken net charges yield a value of 1.3 electrons transferred from the chemisorbed BT_2T_4 to the gold cluster.

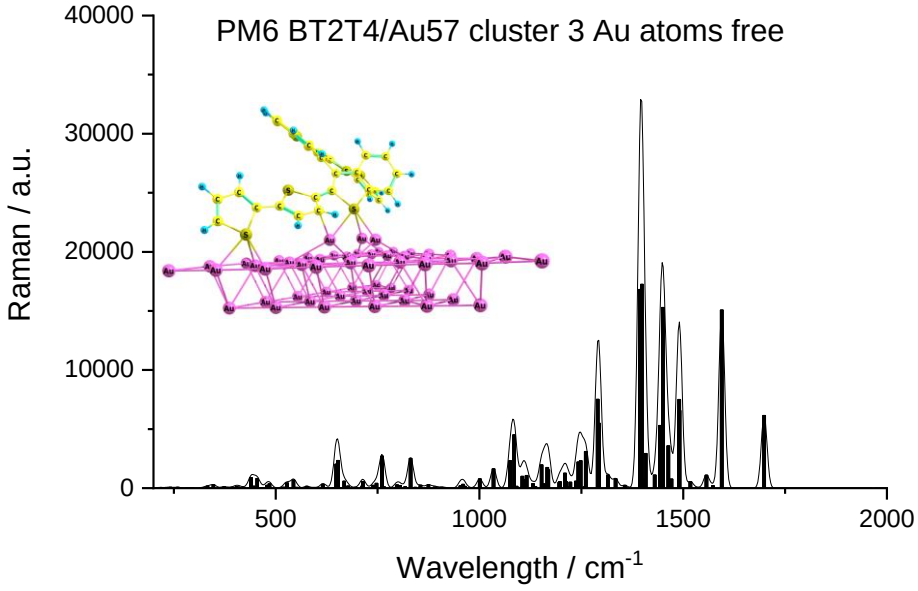

Fig. S10. Theoretical Raman spectra PM6, results of both neutral black (line and bars) and cation red (line and bars).

3.3 Au|BT_2T_4 experimental Raman results

Fig. S11 shows Raman spectra of the Au|BT_2T_4 and Au|BT_2T_4@AgNPs interfaces. Remarkably, a neat difference is found in the spectra as a function of the excitation energy. The use of the 514.5 nm excitation yields a rather noisy spectrum. On the contrary, spectra recorded by using a 785 nm excitation energy, Fig. S11a, feature a much better signal to noise ratio (this peculiar behavior is related to the charge transfer between BT_2T_4 and gold, *vide supra* theoretical results sections 3.1 and 3.2). The intensity of the latter spectra is higher if compared with that of the BT_2T_4 powder. The observation of SERS effect suggests a strong chemisorption of BT_2T_4 on Au, Fig. S11a, and the subsequent chemisorption of AgNPs on top in Fig. S11b. All in all, Raman spectra suggest a strong interaction with both the gold substrate and AgNPs, as well, and that the BT_2T_4 chemisorption is accompanied by a strong charge transfer. In fact, comparison of the absorption spectrum of BT_2T_4 neutral and cation species gives due reason to the difference observed when using the 514.5 nm and 785 nm excitation light sources. Theoretical spectra show that the neutral species absorbs at wavelengths smaller than 450 nm, while the cation has maximum absorption in the 550 to 820 nm range. Thus the absorption of the cation species matches the 785 nm laser excitation energy, which is able to yield good quality Raman spectra.

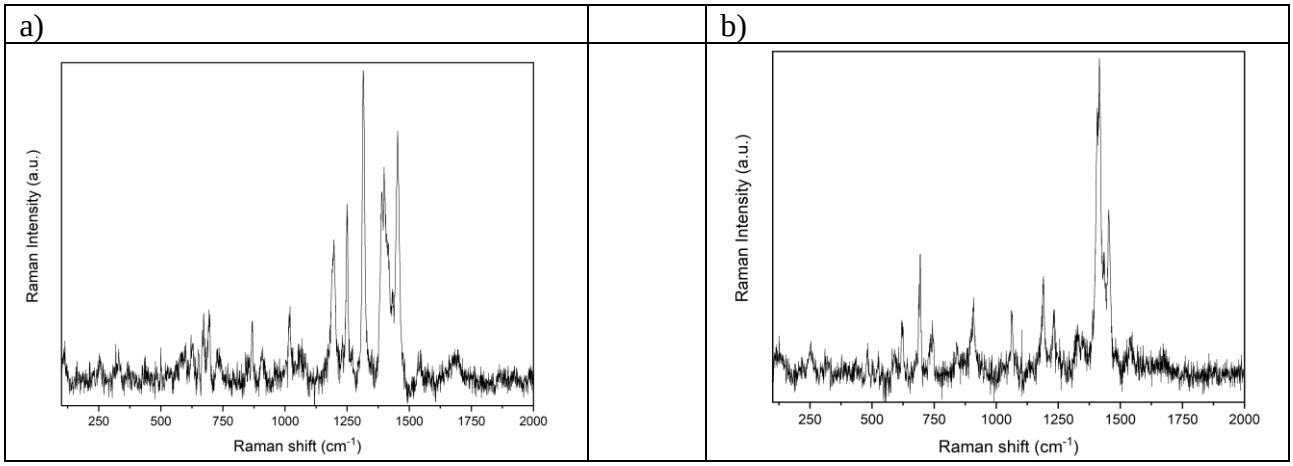

Figure S11. Raman spectra recorded with a 785 nm excitation energy wavelength. a) Au|BT_2T_4 interface. b) Au|BT_2T_4@AgNPs.

3.4 Chiral Ni|BT_2T_4 interface: In-situ electrochemical-Raman characterization

Fig. S12 sets out in-operando Raman spectra, recorded in-situ with the laser focus on the WE in the electrochemical cell of the Ni|BT_2T_4 interface collected as a function of time, while the Ni|BT_2T_4 interface is under potentiostatic reduction regime. Raman spectra were recorded as a function of time at a constant potential of $-0.5\ V$, to maintain Ni in its neutral metallic state (compare section 4.9 of the main manuscript for details concerning the relevant experimental set-up).[12] Fig. S12a shows the Raman spectrum recorded in a wide wavenumber range. Fig. S12b sets out a narrower wavenumber region, which shows a remarkable time evolution. Fig. S12b allows to appreciate a clear-cut increase

in two Raman peaks found at 1517 and 1537 cm^{-1}, vertical dashed line, although they are quite close to a prominent peak of acetonitrile solvent (centered at 1420 cm^{-1}). Remarkably the 1517 and 1537 cm^{-1} peaks increase in intensity at increasing time, whilst the 1420 cm^{-1} is decreasing as the BT_2T_4 increases its surface coverage. Two prominent Raman peaks are found in the theoretical spectrum of the BT_2T_4 cation, vide supra the theoretical results section (Fig.S9 lower panel, cation species, the two peaks at 1519 and 1551 cm^{-1}).

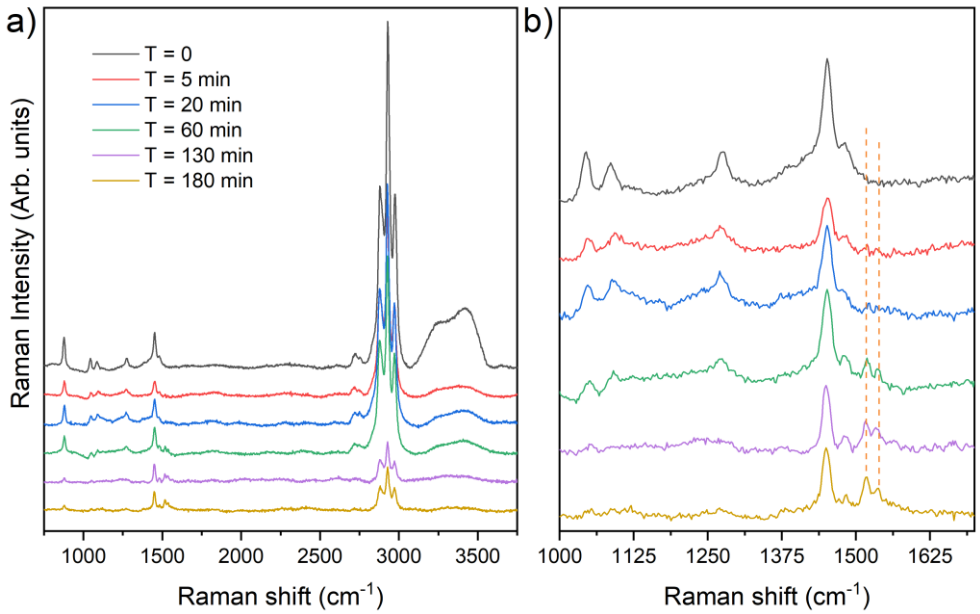

Figure S12. In-situ Raman spectra of the Ni|BT_2T_4 interface, in-operando conditions. The Ni substrate (WE) is maintained at -0.5 V under reduction potentiostatic regime. a) wide wavelength domain b) zoomed region in the 500 – 1800 cm^{-1} wavelength domain.

4) Nickel functionalized surfaces: preparation and characterization.

Ni|BT_2T_4 and Ni|BT_2T_4@AgNPs interfaces were produced with a strategy developed to minimize the Ni oxidation (compare the experimental paragraph, section 4.6 main manuscript).[12]

4.1 Chiral Ni|BT_2T_4 interface: XPS surface characterization

Figure S13 shows XPS spectra of the Ni|BT_2T_4 interface: the survey scan as well as the C 1s, and Ni 2p core level regions. The S 2p photoemission spectrum is shownand discussed in the main manuscript (section 2.2.1).

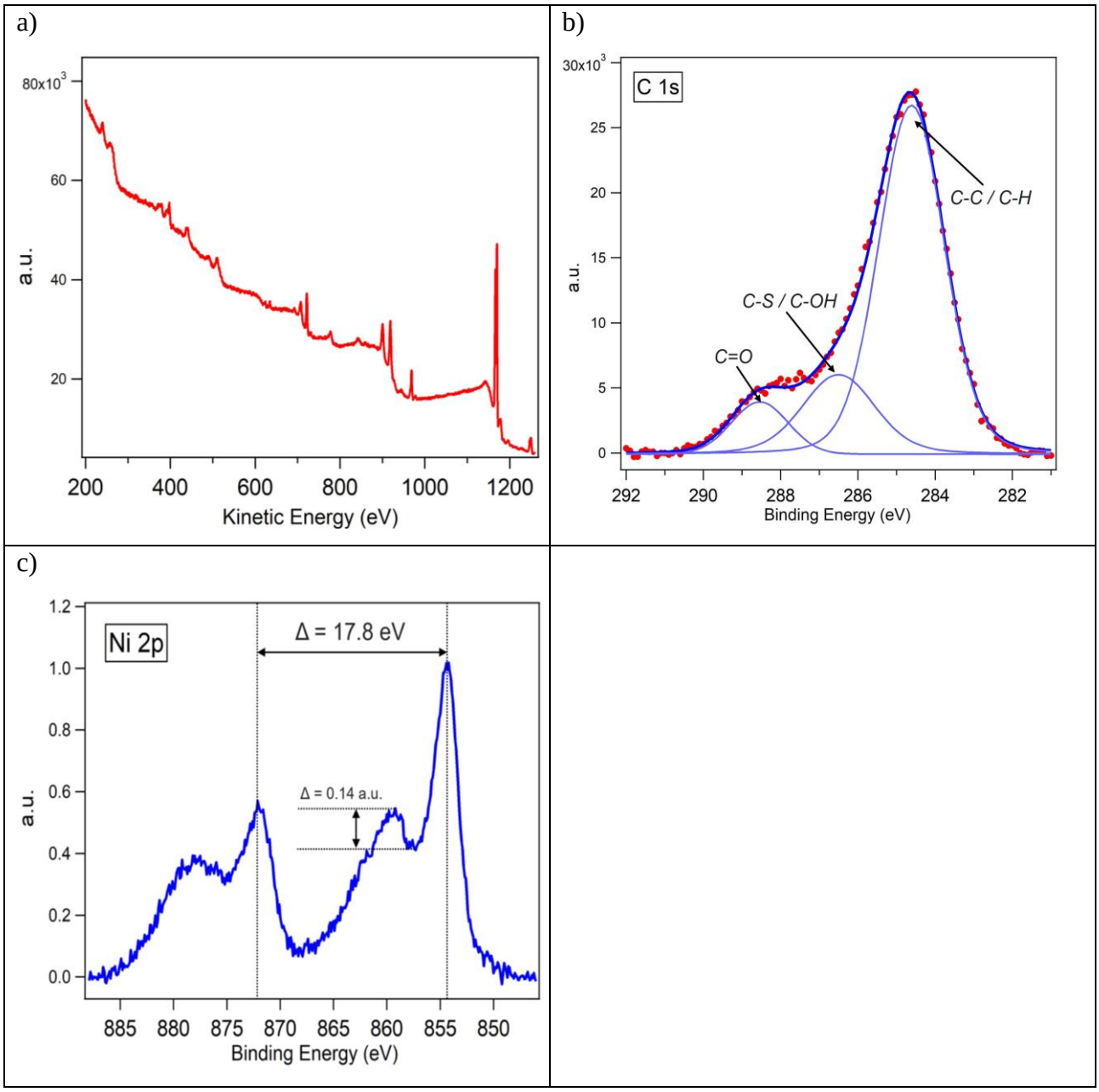

Figure S13. XPS spectra of the Ni|BT_2T_4interface, Mg Kα photons, 1.254 keV photon energy. a) Survey spectrum b) C 1s c) Ni 2p. Panel b): the dotted red curve is the experimental spectrum. Thick blue line overall fit. Thin blue lines are the individual components contribution.

Fig. S13c sets out the XPS spectrum of the Ni 2p core level region, showing a difference in energy between the Ni $2p_{1/2}$ and Ni $2p_{3/2}$ components of 17.8 eV. Suggesting the presence of nickel oxide traces, due to air contamination during the transfer between the electrochemical cell (where the Ni functionalization occurs at a constant reduction potential, i.e. metallic Ni) and the XPS chamber.

4.2 Chiral Ni|BT_2T_4@AgNPs interface: XPS characterization

The Ni|BT_2T_4@AgNPs interface, which is the WE in the Spin-Dependent Electrochemistry measurements in the main manuscript (Experiment II: Fig. 3 b, c) has been characterized via XPS spectroscopy measurements, reported in Fig. S14.

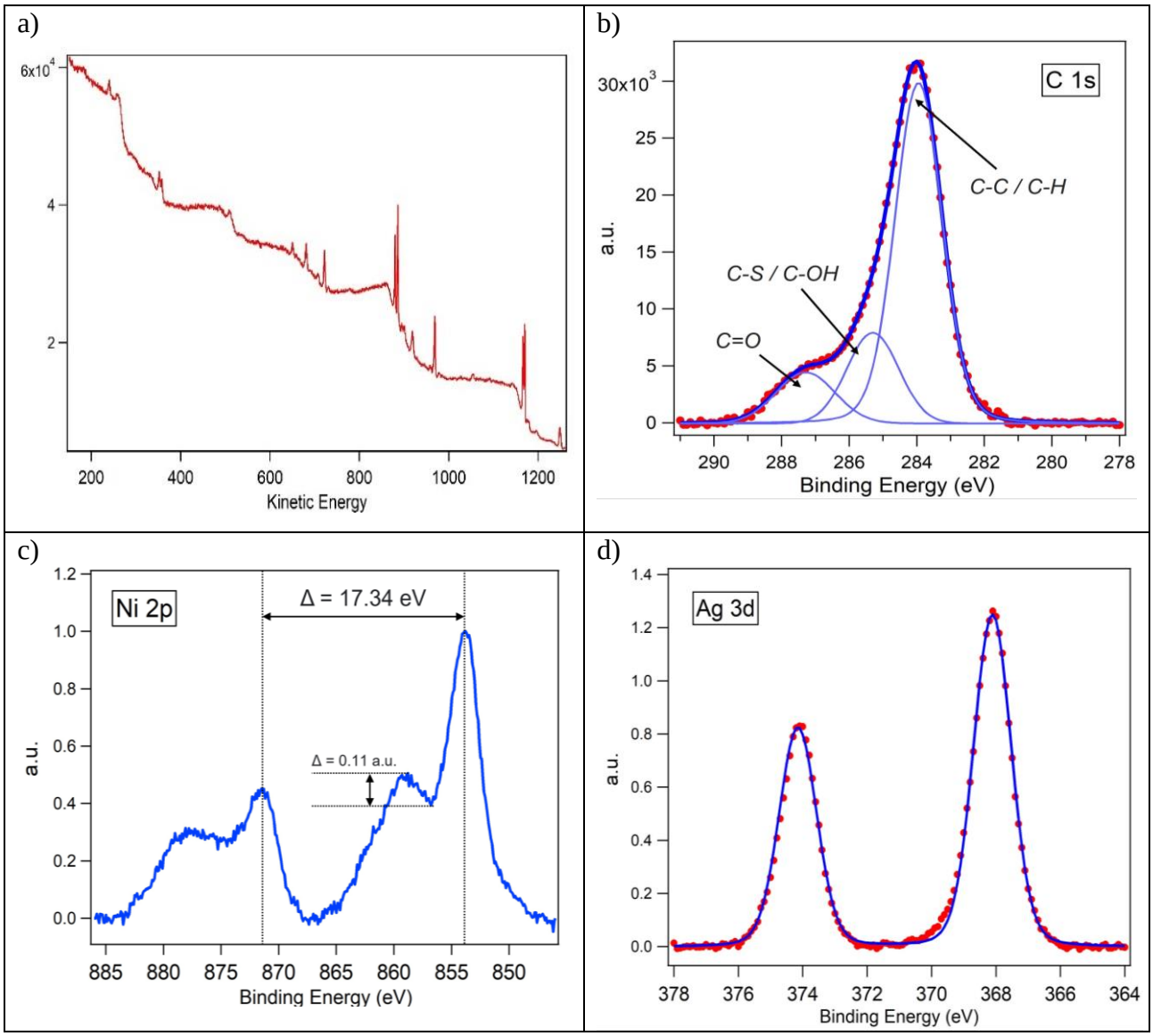

Fig. S14. XPS spectra of the Ni|BT_2T_4|AgNPs interface, Mg Kα photons, 1.254 keV photon energy. a) Survey spectrum b) Ag 3d c) Ni 2p. Panel b): the red dot curve is the experimental spectrum, the blue line is the fitted data.

The survey scan and the C 1s, Ni 2p and Ag 3d core levels are displayed in figure S13a, b, c, d, respectively. The S 2p core level measurements are included and discussed in the main manuscript (section 2.2.1). In the Nickel 2p spectrum (panel c), a difference in energy between the Ni $2p_{1/2}$ and Ni $2p_{3/2}$ components of 17.34 eV is shown, which is slightly lower with respect to the Ni|BT_2T_4 interface (figure S13c). This is an indication of a smaller amount of Nickel oxide.

5) mc-AFM

We investigated the spin selective transport properties through conducting probe AFM where BT_2T_4 molecules of either chirality was self-assembled on gold substrate (Au/Ti/Si: 50nm/10nm/500mm, fabricated by e-beam evaporation). We used a Bruker Scan Analyst system with Co/Cr MESP tips with a spring constant of 0.8nN. We applied Peak Force TUNA mode with a peak force of 20 nN and

a gain of 10 during IV sweeps with a current sensitivity of 100 pA. We found significant differences in the IV curves depending on the direction of the magnetic field and the chirality of the BT_2T_4 molecules, indicating spin filtering effects. The spin polarization was estimated to be about 30% at room temperature, Fig. S15a to d. Fig. S15 shows AFM images of the bare, Fig. S15e and functionalized, Fig. S15f surfaces. The surface morphology is quite similar between bare and functionalized (Au/BT2T4) gold surface.

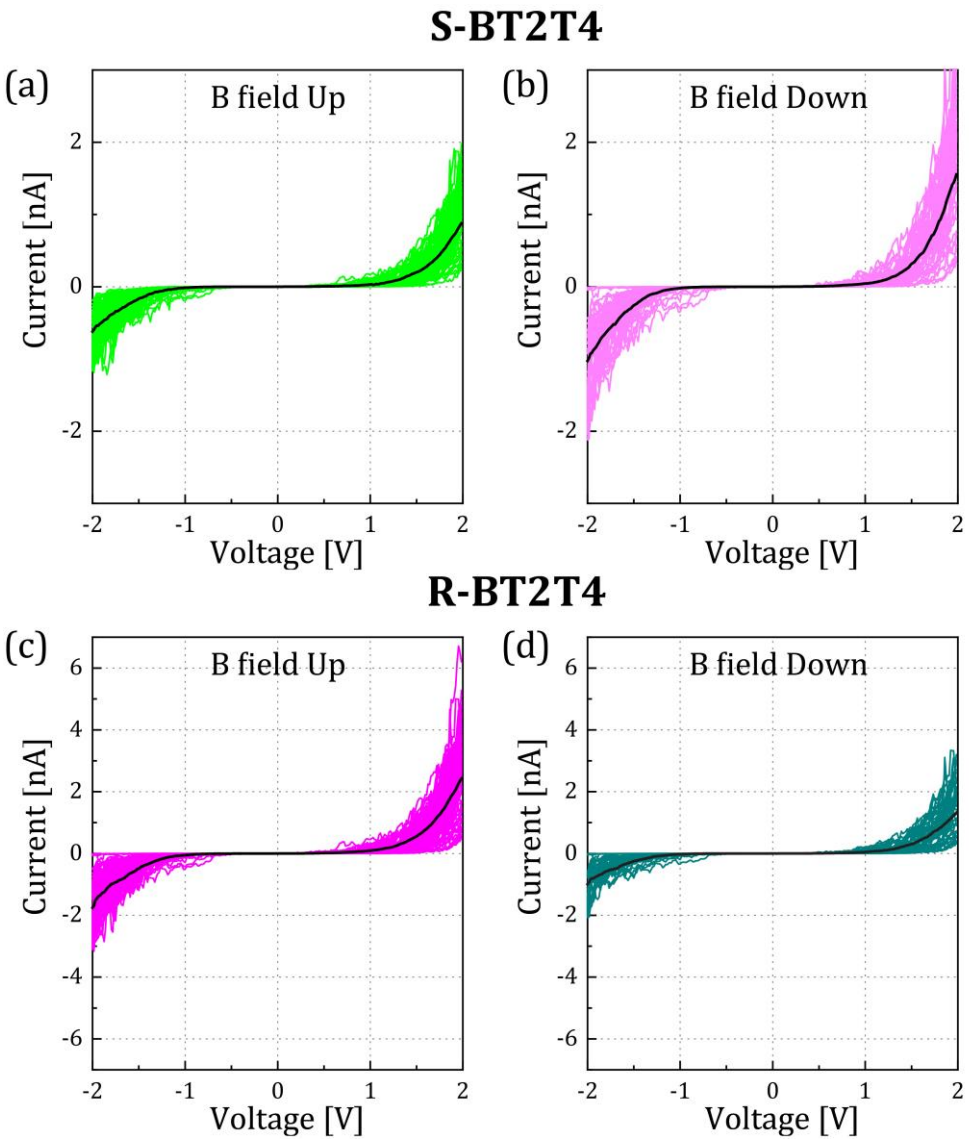

(e) (f)

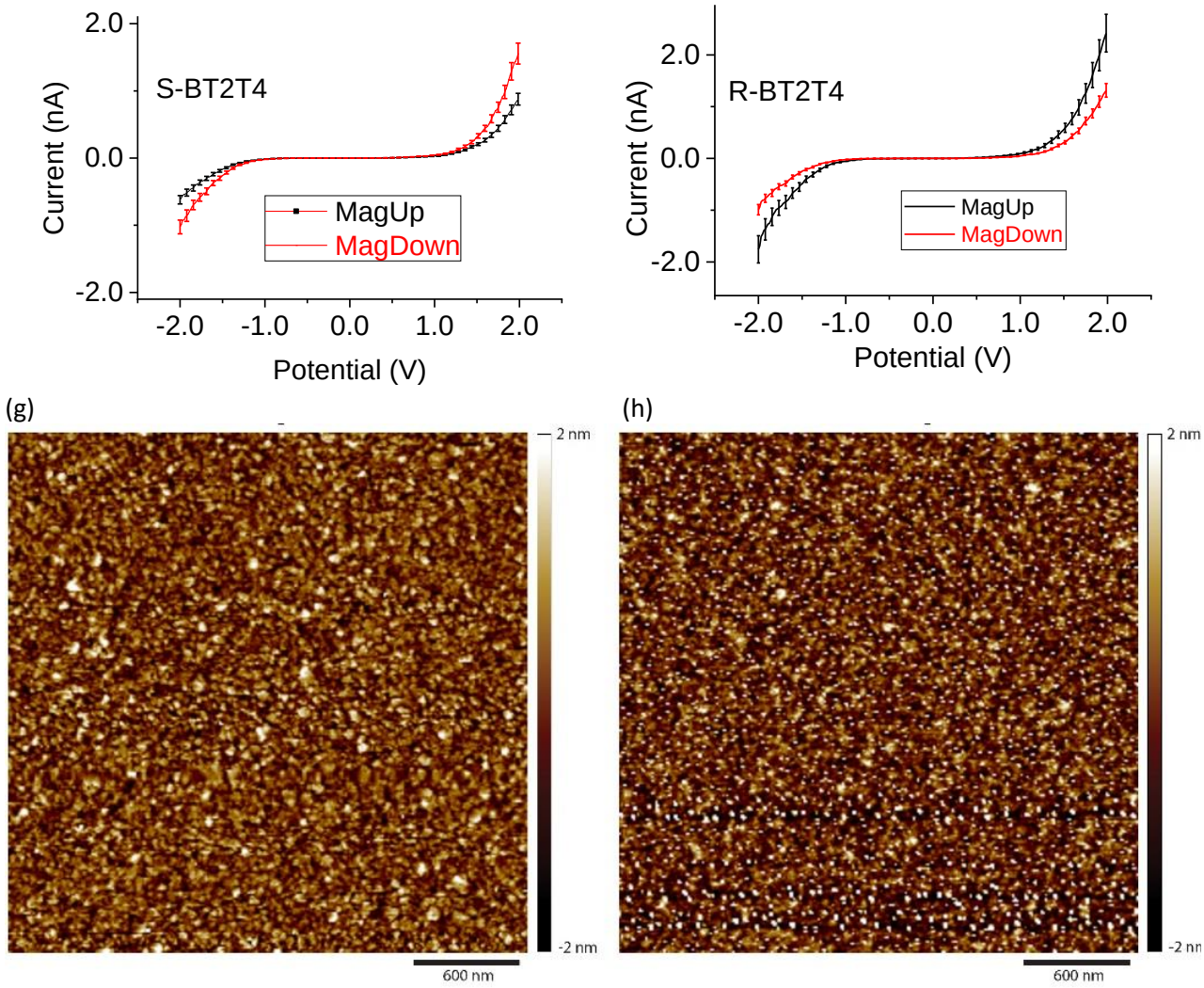

Fig. S15 (a) to (d) Multiple I-V curves recorded on various location of the sample presented in the colored graphs where black lines showing the corresponding average I-V response. Conditions indicated within the figure. (e) and (f) I-V curves with a 15% error bar. (g) and (h) bare gold and BT2T4 SAM on gold surface measured using dynamic mode (peak force QNM) for both the surfaces

Statistical elaboration of the multiple I-V curves indicate a standard deviation just below 5%, which is the sensitivity associated to circle dimensions in the main manuscript Figure 4. Figure S15 (e) and (f) show I-V curves with a 15% error bar, which is a crude and dramatic overestimation of the sensitivity error. Nonetheless, I-V curves recorded as a function of magnet orientation are still neatly discernible.

6) Theoretical results

Theoretical calculations are exploited to provide a molecular based description of the interaction between BT_2T_4 and the Au and Ni surfaces (chemisorption) as well as electronic and spectroscopic properties to be related to the experimental Raman spectroscopy measurements. To this end, both isolated BT_2T_4 theoretical spectra and BT_2T_4 interacting with gold and nickel small clusters have been considered.

6.1 BT_2T_4*/metal cluster*

Gold substrate, PM6 semiempirical calculations have been carried out within a cluster embedded approximation to gain a molecular insight on the BT_2T_4 interaction with gold. The gold surface was simulated by considering a slab of 57 gold atoms, organized in two layers, with a (111) surface orientation. For the sake of comparison two initial guess geometries have been created:

- Parallel, or flat, BT_2T_4 disposition with respect to the gold surface, Fig.S16.
- Perpendicular, or vertical, BT_2T_4 disposition with respect to the gold surface, Fig.S17.

Geometry optimization of the Au|BT_2T_4 cluster shows that BT_2T_4 adsorbs with a "flat" (the BT_2T_4 C2 symmetry axis is parallel to the Au cluster surface) disposition on the surface, maximizing the gold/sulfur interaction, compare Fig. S16b.

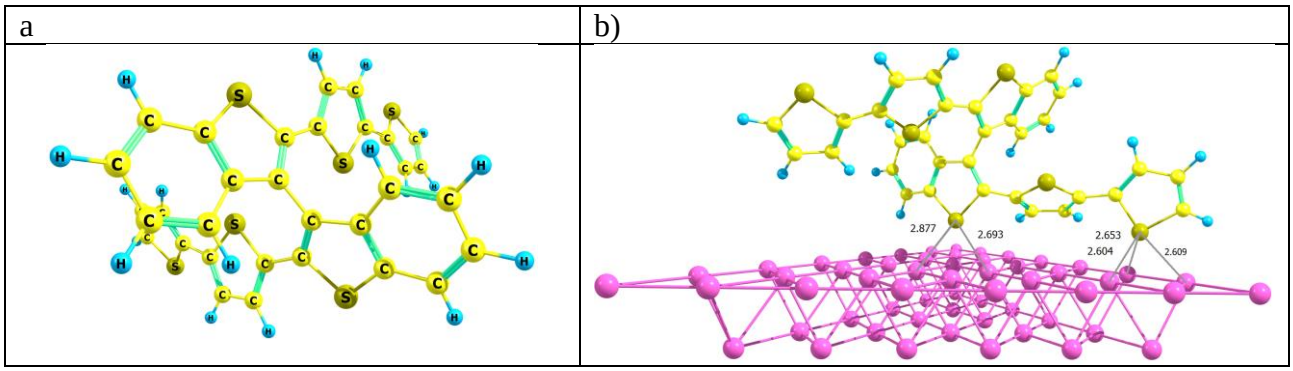

Fig S16. a) (*R*)-BT_2T_4 molecular structure. b) PM6-optimized BT_2T_4 geometry on a fixed-geometry Au (111) 57 atoms slab. Parallel orientation.

Then, the adsorption energy has been calculated as the difference between the Au|BT_2T_4 cluster electronic energy minus that one of the Au(111) slab and adsorbate molecule:

$$E_{ads} = E_{Au_{57}|BT_2T_4} - \left(E_{Au_{57}} + E_{BT_2T_4}\right)$$

Where: E_{ads}, $E_{Au_{57}|BT_2T_4}$, $E_{Au_{57}}$ and $E_{BT_2T_4}$ are the molecular electronic energies of adsorption, Au/BT_2T_4 cluster, Au57 slab and BT_2T_4, respectively. The geometry of the Au(111) slab is kept fixed to that of the experimental crystal,[8] while the geometry of the free isolated BT_2T_4 (relevant to the calculation of E_{BT2T4}) have been fully optimized. In the case of the Au(111)| BT_2T_4 the geometry of the adsorbed thiophene has been fully optimized, while keeping the geometry of the Au(111) slab fixed. The theoretical adsorption energy results -120.1 kcal mol^{-1} for the Au(111)| BT_2T_4 cluster for the parallel (Fig. S16b). The optimized perpendicular orientation geometry, Fig. S17, is found 53 kcal mol^{-1} less stable than the parallel orientation, with an adsorption energy of about 67 kcal mol^{-1}.

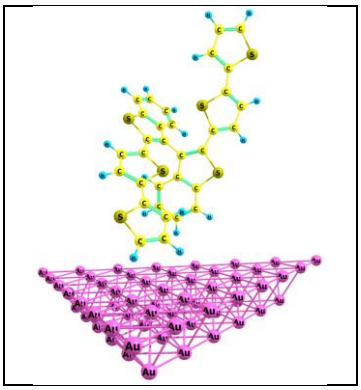

Fig S17. PM6-optimized BT_2T_4 vertical geometry on a fixed-geometry Ni (111) 57 atoms slab.

The adsorption process is driven by the tight interaction, i.e. a short interatomic distance, between the sulfur and Au atoms, with the sulfur "trying" to occupy a hollow adsorption site. A strong charge transfer occurs between the adsorbed molecule and the Au, with a positive Mulliken net charge of 0.4 on the BT_2T_4. Indeed the MOs ordering in energy, of the Au cluster with respect to that of the BT_2T_4 free molecule, shows that the LUMO of the Au cluster is lower in energy with respect to the HOMO of BT_2T_4, Fig. S17. Theoretical facts and figures give strong indication of a chemisorption rather than a pure physisorption. In tight agreement with the experimental outcome: both XPS and Raman results. In particular, a large charge transfer between BT_2T_4 and the Au slab is in agreement with the SERS observed measurements of the BT_2T_4 adsorbed on the Au (vide supra).

A)	b)	c)

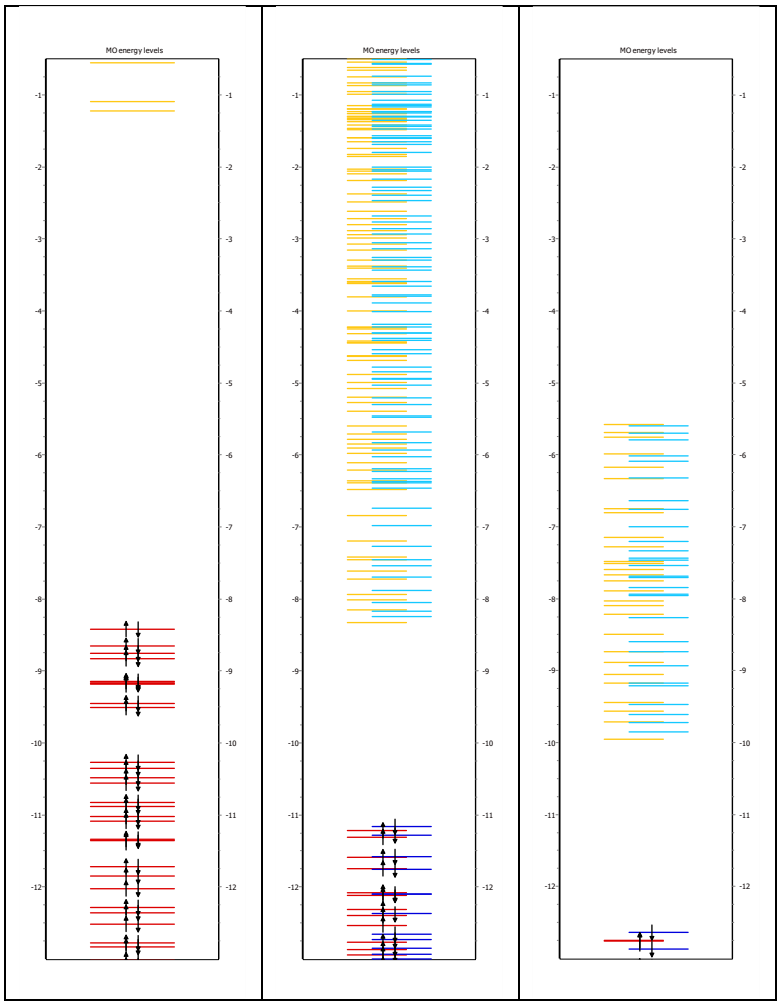

Fig. S18. Correlation diagram MO energies, PM6: a) BT_2T_4 b) Au57(111)|BT_2T_4 c) Au57(111) slab.

Regarding the Nickel substrate: the theoretical adsorption of BT_2T_4 on Ni was modelled following the same approach developed for the Au. The theoretical adsorption energy on Ni results -77.8 kcal mol^{-1} for the Ni(111)| BT_2T_4 cluster, with a charge transfer of 1.4 electrons from BT_2T_4 to Ni, Fig. S17 shows the relevant molecular model. Thus, the adsorption energy of BT_2T_4 on Ni is smaller than for Au. This result is consistent with the bond dissociation energies of sulfur with Au and Ni, 104.2 and 87.5 kcal mol^{-1} respectively.[14]

7) Spin Dependent Electrochemistry setup

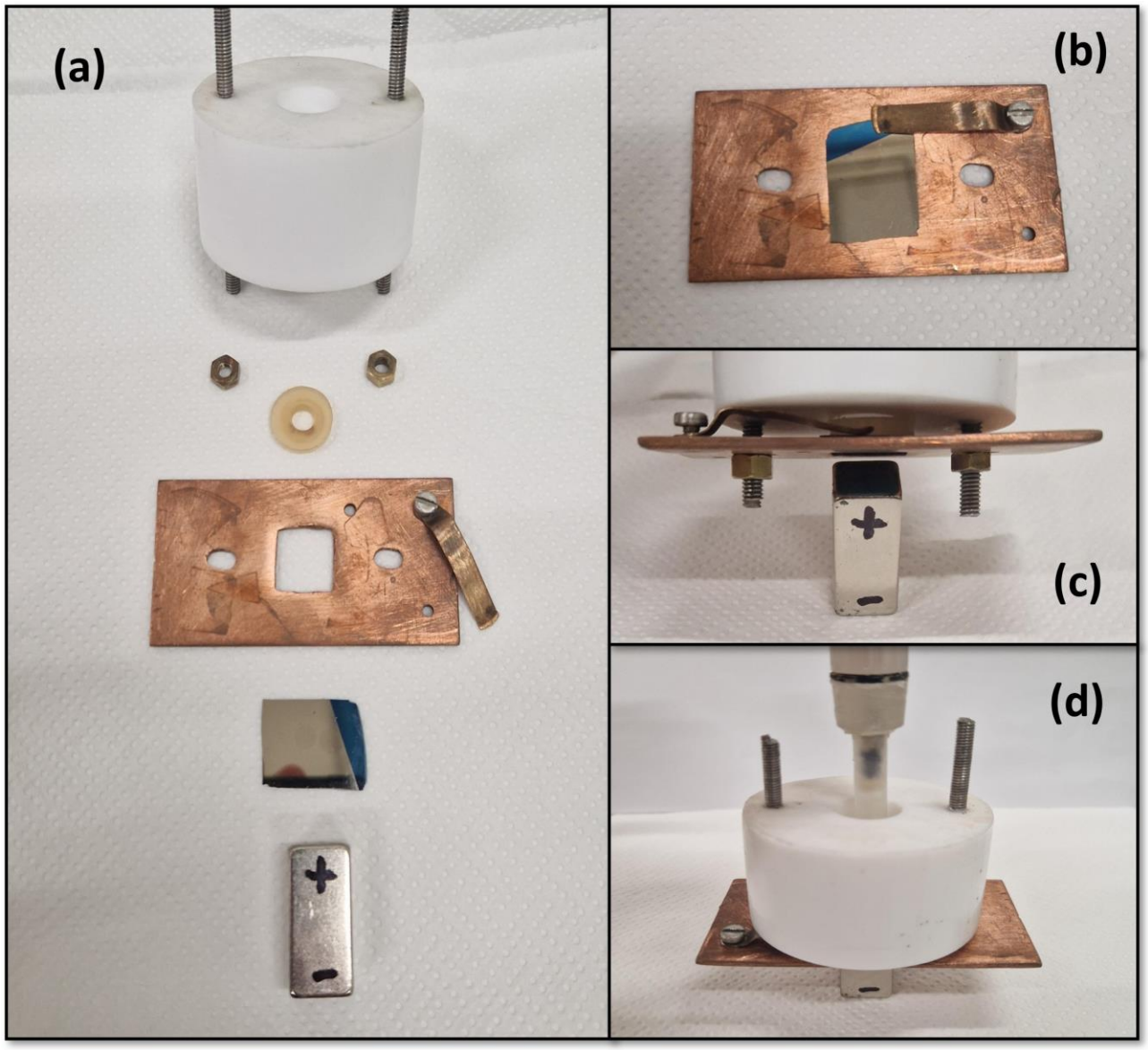

Fig. S19. Spin Dependent Electrochemistry measurements setup. a) Exploded view of the cell and all the involved elements, from below: permanent magnet, nickel electrode, sample holder, o-ring, cell. b) c) d) panels show a sequence of the cell's assembly. The permanent magnet was a NdFeB B88X0 Grade N42 K&J Magnet, Inc., with a nickel coating: magnetic field at the surface is larger than 0.6 T (6353 Gauss).[15]

Reproducibility: CVs and SDE experiments have been replicated a number of times (at least three times), eventually proving that the current vs. potential curves are affected by an overall confidence interval of $\pm 1\%$.

References

(1) Chateau, D.; Liotta, A.; Gregori, D.; Lerouge, F.; Chaput, F.; Desert, A.; Parola, S. Controlled Surface Modification of Gold Nanostructures with Functionalized Silicon Polymers. *J Sol-Gel Sci Technol* **2017**, *81* (1), 147–153. https://doi.org/10.1007/s10971-016-4116-y.

(2) Starowicz, M.; Stypu\la, B.; Banaś, J. Electrochemical Synthesis of Silver Nanoparticles. *Electrochemistry communications* **2006**, *8* (2), 227–230.
(3) Tassinari, F.; Tancini, E.; Innocenti, M.; Schenetti, L.; Fontanesi, C. On the Hybrid Glassy Carbon Electrode/OligoThiophene/Ag(NP) Interface. *Langmuir* **2012**, *28* (44), 15505–15512. https://doi.org/10.1021/la3025777.
(4) Choi, Y.-J.; Luo, T.-J. M. Electrochemical Properties of Silver Nanoparticle Doped Aminosilica Nanocomposite. *International Journal of Electrochemistry* **2011**, *2011*, e404937. https://doi.org/10.4061/2011/404937.
(5) Liu, F.; Huang, L.; Duan, X.; Li, Y.; Hu, J.; Li, B.; Lu, J. A Facile Method to Prepare Noble Metal Nanoparticles Modified Self-Assembly (SAM) Electrode. *Journal of Experimental Nanoscience* **2018**, *13* (1), 1–10. https://doi.org/10.1080/17458080.2017.1373202.
(6) Ulman, A. *An Introduction to Ultrathin Organic Films, 1st Edition, Academic Press, Boston, 1991*. http://store.elsevier.com/product.jsp?isbn=9780127082301&_requestid=130432 (accessed 2013-11-06).
(7) Finklea, H. O. Self-Assembled Monolayers on Electrodes. In *Encyclopedia of Analytical Chemistry*; John Wiley & Sons, Ltd, 2006.
(8) Maeland, A.; Flanagan, T. B. Lattice Spacings of Gold–Palladium Alloys. *Can. J. Phys.* **1964**, *42* (11), 2364–2366. https://doi.org/10.1139/p64-213.
(9) Powell, C. J.; Jablonski, A. Evaluation of Calculated and Measured Electron Inelastic Mean Free Paths Near Solid Surfaces. *Journal of Physical and Chemical Reference Data* **1999**, *28* (1), 19–62. https://doi.org/10.1063/1.556035.
(10) Seah, M. P.; Dench, W. A. Quantitative Electron Spectroscopy of Surfaces: A Standard Data Base for Electron Inelastic Mean Free Paths in Solids. *Surface and Interface Analysis* **1979**, *1* (1), 2–11. https://doi.org/10.1002/sia.740010103.
(11) Jablonski, A.; Powell, C. J. Relationships between Electron Inelastic Mean Free Paths, Effective Attenuation Lengths, and Mean Escape Depths. *Journal of Electron Spectroscopy and Related Phenomena* **1999**, *100* (1), 137–160. https://doi.org/10.1016/S0368-2048(99)00044-4.
(12) Fontanesi, C.; Tassinari, F.; Parenti, F.; Cohen, H.; Mondal, P. C.; Kiran, V.; Giglia, A.; Pasquali, L.; Naaman, R. New One-Step Thiol Functionalization Procedure for Ni by Self-Assembled Monolayers. *Langmuir* **2015**, *31* (11), 3546–3552. https://doi.org/10.1021/acs.langmuir.5b00177.
(13) Jiang, T.; Koshmak, K.; Giglia, A.; Banshchikov, A.; Sokolov, N. S.; Dinelli, F.; Capelli, R.; Pasquali, L. Controlling In-Plane Isotropic and Anisotropic Orientation of Organic Semiconductor Molecules on Ionic Fluoride Dielectrics. *J. Phys. Chem. C* **2017**, *121* (8), 4426–4433. https://doi.org/10.1021/acs.jpcc.6b12926.
(14) Speight, J. *Lange's Handbook of Chemistry, Seventeenth Edition*.
(15) Gazzotti, M.; Arnaboldi, S.; Grecchi, S.; Giovanardi, R.; Cannio, M.; Pasquali, L.; Giacomino, A.; Abollino, O.; Fontanesi, C. Spin-Dependent Electrochemistry: Enantio-Selectivity Driven by Chiral-Induced Spin Selectivity Effect. *Electrochimica Acta* **2018**, *286*, 271–278. https://doi.org/10.1016/j.electacta.2018.08.023.